Title
Lateral opening of a translocon upon entry of protein suggests the mechanism of insertion into membranes

Journal
Proceedings of the National Academy of Sciences of the United States of America, 107(40)

ISSN
0027-8424

Authors
Egea, Pascal F
Stroud, Robert M

Publication Date
2010-10-05

DOI
10.1073/pnas.1012556107

Peer reviewed

Supporting Information

Egea and Stroud 10.1073/pnas.1012556107

SI Materials and Methods

Protein Expression and Purification. The three genes encoding the SecY (PF1989), SecE (PF1801), and Sec61β (PF2016) subunits of the translocon from *Pyrococcus furiosus* were cloned by PCR using total genomic DNA (ATCC reference strain). The three genes were inserted in tandem by oriented quadruple ligation in a modified pBAD expression vector (Invitrogen). In our expression construct, the SecY gene was expressed as a C-terminal histidine-tagged fusion protein with a thrombin cleavage site allowing copurification of the heterotrimeric SecYEβ complex. Each gene was cloned with an independent ribosomal binding site but placed under the control of a single and tightly regulated arabinose promoter (1). The natural SecY gene sequence was later replaced with a synthetic gene after codon optimization for its expression in *Escherichia coli*. Proteins were coexpressed using the BL21(AI) *E. coli* strain grown in LB medium at 37 °C for 4 h and 0.2% arabinose as an inducer. Seleno-methionine–labeled protein was expressed in a modified M9 medium (2, 3) using 2% glycerol as the carbon source. There are no mutations in the expression construct used in this study.

Cells were lysed using an emulsiflex homogenizer, and membrane fractions were prepared by differential ultracentrifugation. Membranes solubilized using n-dodecyl-β-D-maltopyranoside (DDM) and n-octyl-β-D-glucopyranoside (OG) were clarified by selective heat precipitation. Purification of the *Pyrococcus furiosus* (*Pfu*)-SecYEβ protein-detergent complex was achieved in three steps combining nickel-chelating affinity chromatography, gel filtration, and cation-exchange chromatography after thrombinolysis of the hexa-histidine purification tag. The purified species was identified as a monomeric heterotrimeric complex of SecYEβ with an apparent 1:1:1 stoichiometry. The presence of all three subunits was confirmed by gel electrophoresis and MALDI-TOF MS.

Crystallization. High-throughput crystallization screening of *Pfu*-SecYEβ stabilized in OG was performed using a nanoliter robotic workstation Mosquito (TTP LabTech) by vapor diffusion in hanging drop setups at 4 °C and the sampling of 768 conditions. Although several crystallization conditions were obtained, the best crystals of *Pfu*-Sec61 grew in 15–25% PEG 4,000 or PEG 8,000, 50–125 mM magnesium or calcium acetate, and 100 mM Mes (pH 5.5–6.5). Optimization required a combination of additive screening and macroseeding. Crystals belong to space group $C222_1$ with one SecYE complex per asymmetric unit and a solvent content of about 70%. The Sec61β subunit was lost during the course of crystallization. Crystals diffracted anisotropically to 3.5-Å resolution in the case of the seleno-labeled protein. Native crystals eventually diffracted at 2.9 Å. However, completeness and mean $I/\sigma(I)$ drop drastically beyond 3.15 Å. Final data were integrated, scaled, and reduced to 2.9-Å resolution; the corresponding statistics are shown in Tables S1–S3. As maximum likelihood-based phasing and refinement methods weigh reflections according to measurement accuracy using a probabilistic approach, all observed reflections (up to 3.5-Å resolution) were included during the refinement against the final native dataset.

Data Collection and Structure Determination, Refinement, and Validation. X-ray diffraction data were collected at beamline 8.3.1 at the Advanced Light Source using a Quantum Q315r CCD detector. Crystals were flash-frozen in liquid nitrogen using mother liquor supplemented with 25% glycerol or ethylene glycol as a cryoprotectant. A single crystal of selenium-labeled protein was used to collect two separate datasets: a single anomalous dispersion dataset collected at the peak energy and a multiple anomalous dispersion at two wavelengths corresponding to the inflection and remote energies. These data were indexed, scaled, and reduced using *MOSFLM* (4) and *Scala* (5) in *Elves* (6) and *HKL2000* (7). Phasing was achieved using a combination of molecular replacement using a minimalist model corresponding to the SecYE core of the *Methanococcus jannaschii* (*Mja*)-SecYEβ (8) with all its loops deleted and thermal B-factors adjusted at 130 $Å^2$, and the anomalous signal was extracted from the multiwavelength anomalous dispersion dataset. Molecular replacement (MR) using *Phaser* (9) in *Phenix* (10) and the dataset collected at the excitation peak wavelength yielded a solution (Z score = 7.6 and likelihood = 116 for the full atom model and Z score = 6.4 and likelihood = 124 for the poly-alanine model) with convincing electron density maps.

Refinement of low-resolution structures from a good starting model (as it is the case for molecular replacement searches using a high-resolution structure) tends to give lower R factors than structures based on experimental phasing. However, refinement based solely on the molecular replacement solution proved impossible in our case. This is because of the rather poor quality of the initial anomalous dataset. To prevent model bias that can be significant at this intermediate resolution, it was essential to use the anomalous dispersion signal to improve phasing. Attempts to phase using a single wavelength anomalous dispersion (SAD) approach failed, whereas the multiwavelength anomalous dispersion (MAD) strategy succeeded. Phasing and density modification/improvement cycles were performed combining phase information from molecular replacement and anomalous dispersion. Anomalous Fourier difference maps contoured at 4σ and calculated using the phases from the initial molecular replacement solution using all atoms or simplified to a poly-alanine backbone were visually inspected to eventually assign six sites corresponding to residues Met31/(Lys28), Met121/(Met118), *Met150*/(Val143), *Met241*/(Ile210), *Met260*/(Met229), and *Met458*/(Leu426) from the SecY subunit in *Pfu*/*(Mja*). Methionines 150, 241, 260, and 458 were unambiguous. Although the two additional sites corresponding to Met156/(Phe149) and Met49/(Tyr54), respectively belonging to the Y and E subunits, could not be identified initially, these weaker sites were eventually assigned and were useful to sequence assignment during model building (Fig. S2). MR-MAD combined phasing and density modification were then carried out in *Phenix* using *Solve*/*Resolve* and assuming a solvent percentage of 65% with a single copy of SecYE in the asymmetric unit. Automatic building in *Phenix* was efficient to rebuild some of the membrane-spanning helices as poly-alanine helices. The MAD dataset was used to determine initial experimental phases and perform a single cycle of manual building and refinement to enforce proper sequence register. Helix register and sequence assignment were established using the MR/MAD phases obtained with the poly-alanine search model. As a control, refinement was carried out simultaneously and independently against the two sets of experimental phases determined in *Solve* before or after statistical density modification in *Resolve*. At this stage, all transmembrane helices (TM) segments of the channel were placed, and the positions of selenium sites were used to assign the proper sequence register. The initial experimentally phased map showed clear density corresponding to the αC-terminal helix that contained the residue Met458 specific to *Pfu* (Movie S1). Furthermore, whereas the molecular replacement model did not contain the entire TM6, the resulting maps restituted the corresponding density. Considering only the data collected at the remote and

inflection, a completeness of 80% is a reasonable compromise, allowing reliable determination of experimental phases; data collected at the peak have stronger mean $I/\sigma(I)$ but suffered from lack of completeness. Refinement and model regularization were done using *Phenix*, *CNS* (11, 12), and *REFMAC* (13); model building was performed in *COOT* (14). Despite limited resolution, strong anisotropy, and poor completeness in the highest resolution shells, the anomalous dataset allowed refinement of the model to R_{free} and R_{cryst} values of 39.3% and 37.5%, respectively, and a maximum of likelihood-based overall figure of merit of 0.70. All TM segments and the αC-terminal helix were assigned at this stage of structure determination. The anomalous data were not corrected for anisotropic diffraction.

A single native crystal was used to collect the final dataset, showing severe anisotropic diffraction up to 2.9-Å resolution. Data were processed up to 2.9-Å resolution using *XDS* (1517), and the detailed statistics are given in Table S1. However, for the sake of rigorousness, we first limited the resolution to 3.5 Å to carry the refinement of the structure to R_{free} and R_{cryst} values of 38.0% and 35.3%, with an overall B factor of 140 $Å^2$ in relative agreement with the estimated apparent B_{Wilson}. When thermal factors were sharpened by a factor of −52.5 $Å^2$, as determined in *CNS*, the resulting maps showed improvement and could be used to guide manual building. Analysis of the X-ray data anisotropy was done using the server http://www.doe-mbi.ucla.edu/~sawaya/anisoscale/, which performs ellipsoidal truncation and anisotropic scaling (18). When applying a strict cutoff of $F/\sigma(F) = 3.0$, the recommended resolution limits along reciprocal axis a^*, b^*, and c^* were 3.3, 4.1, and 2.9 Å, respectively; this corresponded to an overall severe anisotropic correction of 64.6 $Å^2$. From the 24,232 reflections present in the native dataset, 7,649 were discarded, because they fell outside the specified ellipsoid with dimensions 1/3.3, 1/4.1, and 1/2.9 $Å^{-1}$ along a^*, b^*, and c^*, respectively. The discarded reflections still had an average $F/\sigma(F)$ of 2.71. Thus, 16,583 reflections remained after ellipsoidal truncation. After anisotropic scale factors were applied to remove anisotropy from the dataset, an isotropic thermal factor of −76.5 $Å^2$ was applied to restore the magnitude of the high-resolution reflections diminished by the anisotropic scaling procedure. Refinement included rigid body refinement to adjust the position of the TM segments and simulated annealing torsion angle refinement, including restraints to enforce proper α-helical geometry of TMs and thorough estimation of the solvent mask in *Phenix*. Final refinement cycles were carried in *Buster-TNT* (19) to complete the structure with final R_{free} and R_{cryst} values of 31.7% and 27.7%, respectively.

The *MolProbity* (20) and *Polygon* (21) validation tools were used to assess the quality of the final model and show that, despite its modest resolution, our structure falls within the average distribution of X-ray structures deposited in the Protein Data Bank and stands comparison with other translocon structures solved at similar resolution (PDB entries 1RH5, 2YXQ, 2YXR, and 2ZJS). The final structure shows disorder in regions corresponding to residues 1–25, 91–113, 139–144, 265–276, 380–388, and 401–406 that lacked interpretable density and were not built. With 78 of the 468 residues constituting the *Pfu*-SecY subunit poorly ordered, 16% of the structure are not modeled; combined with the severe anisotropy of the diffraction data, this can partially account for the final R_{free}/R_{cryst} values. Our discussion is based on the analysis of TM positioning and rearrangement and the observation of the C-terminal helix of SecY. All these secondary structure elements were assigned using experimental phases. We do not pretend to analyze, in detail, hydrogen-bonding networks to explain opening of the channel, because the resolution of the present structure does not allow it.

In Vivo Complementation Assay and Expression of SecY Complexes. *Pfu*-SecY and *E. coli* (*Ec*)-SecY C-terminal deletion mutants corresponding to *Pfu*-YΔ (encoding Met1-Glu453) or *Ec*-YΔ (encoding Met1-Leu423) were engineered; they, respectively, lacked the 15 and 20 C-terminal residues corresponding to the terminal part of the cytoplasmic helix αC in the *Pfu*-SecY structure. Point mutants of *Pfu*-SecY were generated at positions E457A, F459A, R463A, and K464A (mapping on the cytoplasmic C-terminal helix of *Pfu*-SecY) together with the double mutants R463A/K464A and F459P/A461P. The thermosensitive *E. coli* mutant strain DHB7302 (22) derived from strain IQ85 [genotype F^-. araD139 . DE(argF-lac)169 . l^-. flhD5301 . DE(fruK-yeiR)725(fruA25) . relA1 . secY24 (ts) . rpsE0(SpcR) . zhe-33::Tn10 . rpsL999(StrR) . rbsR22 . DE (fimB-fim)632(::IS1) . deoC1] (23, 24) was transformed with different pBAD vectors with no insert or gene clusters encoding the *E. coli*-SecYEG or *Pfu*-SecYEβ corresponding complexes. Cells were first plated on NZ medium before restreaking on M9-glycerol medium at two temperatures (permissive 37 °C or nonpermissive 42 °C); each test was performed in triplicate. Despite the absence of arabinose, the basal expression of the wild-type *Pfu*-SecY or *E. coli*-SecY genes placed under control of the arabinose promoter at levels essentially equivalent to the chromosomal copy of SecY explains their ability to complement the deficient strain at the nonpermissive temperature. Wild-type and truncation mutants were coexpressed in *E. coli* and purified in DDM and OG using similar procedures (Fig. S4).

1. Guzman LM, Belin D, Carson MJ, Beckwith J (1995) Tight regulation, modulation, and high-level expression by vectors containing the arabinose PBAD promoter. *J Bacteriol* 177:4121–4130.
2. Doublié S (1997) Preparation of selenomethionyl proteins for phase determination. *Methods Enzymol* 276:523–530.
3. Studier FW (2005) Protein production by auto-induction in high density shaking cultures. *Protein Expr Purif* 41:207–234.
4. Leslie AG (2006) The integration of macromolecular diffraction data. *Acta Crystallogr D Biol Crystallogr* 62:48–57.
5. Collaborative Computational Project, Number 4 (1994) The CCP4 suite: Programs for protein crystallography. *Acta Crystallogr D Biol Crystallogr* 50:760–763.
6. Holton J, Alber T (2004) Automated protein crystal structure determination using ELVES. *Proc Natl Acad Sci USA* 101:1537–1542.
7. Otwinowski Z, Minor W (1997) Processing of x-ray diffraction data collected in oscillation mode. *Methods Enzymol* 276:305–326.
8. Van den Berg B, et al. (2004) X-ray structure of a protein-conducting channel. *Nature* 427:36–44.
9. McCoy AJ, et al. (2007) Phaser crystallographic software. *J Appl Crystallogr* 40: 658–674.
10. Adams PD, et al. (2002) PHENIX: Building new software for automated crystallographic structure determination. *Acta Crystallogr D Biol Crystallogr* 58:1948–1954.
11. Brünger AT, et al. (1998) Crystallography & NMR system: A new software suite for macromolecular structure determination. *Acta Crystallogr D Biol Crystallogr* 54: 905–921.
12. Brunger AT, DeLaBarre B, Davies JM, Weis WI (2009) X-ray structure determination at low resolution. *Acta Crystallogr D Biol Crystallogr* 65:128–133.
13. Murshudov GN, Vagin AA, Dodson EJ (1997) Refinement of macromolecular structures by the maximum-likelihood method. *Acta Crystallogr D Biol Crystallogr* 53: 240–255.
14. Emsley P, Cowtan K (2004) Coot: Model-building tools for molecular graphics. *Acta Crystallogr D Biol Crystallogr* 60:2126–2132.
15. Kabsch W (1988) Evaluation of single-crystal X-ray diffraction data from a position-sensitive detector. *J Appl Crystallogr* 21:916–924.
16. Kabsch W (1988) Automatic indexing of rotation diffraction patterns. *J Appl Crystallogr* 21:61–72.
17. Kabsch W (1993) Automatic processing of rotation diffraction data from crystals of initially unknown symmetry and cell constants. *J Appl Crystallogr* 26:795–800.
18. Strong M, et al. (2006) Toward the structural genomics of complexes: Crystal structure of a PE/PPE protein complex from Mycobacterium tuberculosis. *Proc Natl Acad Sci USA* 103:8060–8065.
19. Blanc E, et al. (2004) Refinement of severely incomplete structures with maximum likelihood in BUSTER-TNT. *Acta Crystallogr D Biol Crystallogr* 60:2210–2221.
20. Davis IW, et al. (2007) MolProbity: All-atom contacts and structure validation for proteins and nucleic acids. *Nucleic Acids Res* 35:W375–W383.
21. Urzhumtseva L, Afonine PV, Adams PD, Urzhumtsev A (2009) Crystallographic model quality at a glance. *Acta Crystallogr D Biol Crystallogr* 65:297–300.
22. Li W, et al. (2007) The plug domain of the SecY protein stabilizes the closed state of the translocation channel and maintains a membrane seal. *Mol Cell* 26:511–521.

23. Shiba K, Ito K, Yura T, Cerretti DP (1984) A defined mutation in the protein export gene within the spc ribosomal protein operon of Escherichia coli: Isolation and characterization of a new temperature-sensitive secY mutant. *EMBO J* 3:631–635.

24. Shiba K, Ito K, Yura T (1984) Mutation that suppresses the protein export defect of the secY mutation and causes cold-sensitive growth of Escherichia coli. *J Bacteriol* 160: 696–701.

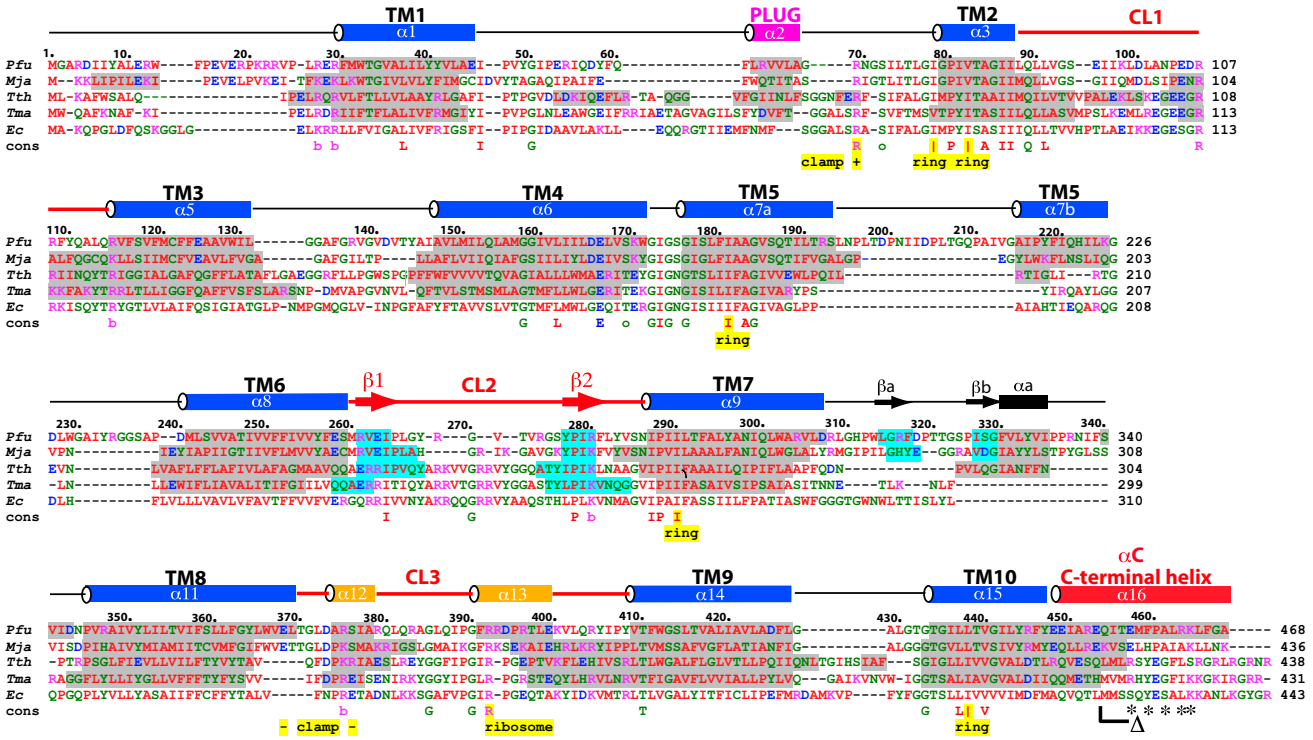

Fig. S1. 3D structure-based sequence alignment of SecY subunits of known structure. *Pyrococcus furiosus*, *Methanococcus jannaschii*, *Thermotoga maritima*, *Thermus thermophilus*, and *Escherichia coli* sequences are aligned. The secondary structure elements of *Pfu*-SecY are indicated. The 10 transmembrane helices (TMs) and three of four cytoplasmic loops (CL) are labeled. All helices are also labeled from α1 to α16. TM helices and cytoplasmic regions are colored in blue and red, respectively. Sequences corresponding to α-helices or β-sheets are, respectively, shaded in gray and cyan. The plug and the C-terminal docking helices are highlighted. Residues that constitute the hydrophobic ring seal are labeled. Residues contributing to ribosome binding are indicated. Residues constituting the clamp involved in electrostatic interactions with the charges flanking the core of signal sequences are labeled. Conserved residues and the strict sequence consensus are indicated in bold. Δ indicates the αC-terminal deletion tested for the complementation, whereas point mutations E457A, F459A, F459P, A461P, R463A, and K464A are marked with an asterisk. More extensive sequence alignments have been reported (1, 2).

1. Van den Berg B, et al. (2004) X-ray structure of a protein-conducting channel. *Nature* 427:36–44.
2. Bondar AN, del Val C, Freites JA, Tobias DJ, White SH (2010) Dynamics of SecY translocons with translocation-defective mutations. *Structure* 18:847–857.

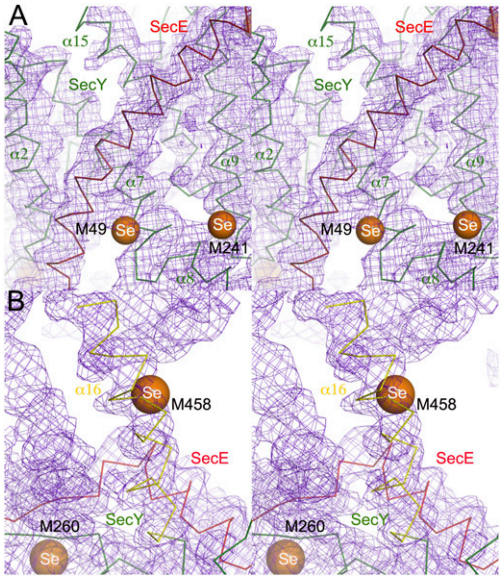

Fig. S2. Experimental phasing. Two stereo views of the initial likelihood-weighted 2mFo-DFc Fourier difference electron density map contoured at 1.1σ after MR-MAD phasing and density modification at 3.5-Å resolution. The selenium sites are indicated as orange spheres. Subunits Y and E are, respectively, colored in green and red. (*A*) Position assignment of methionines. The backbone trace corresponds to the initial partial molecular replacement solution found using a truncated version of the *Mja*-SecYE core. Residues Met49 (in SecE) and Met241 (in SecY; *Pfu* numbering) correspond to methionine residues in *Pfu* that are not methionines in *Mja*. Their assignment is based on analysis of anomalous Fourier difference maps. (*B*) A long cytoplasmic C-terminal helix. The previously unseen C-terminal helix (αC) with the selenium site corresponding to Met458 is shown. The protein trace shown corresponds to the first cycle of manual model building.

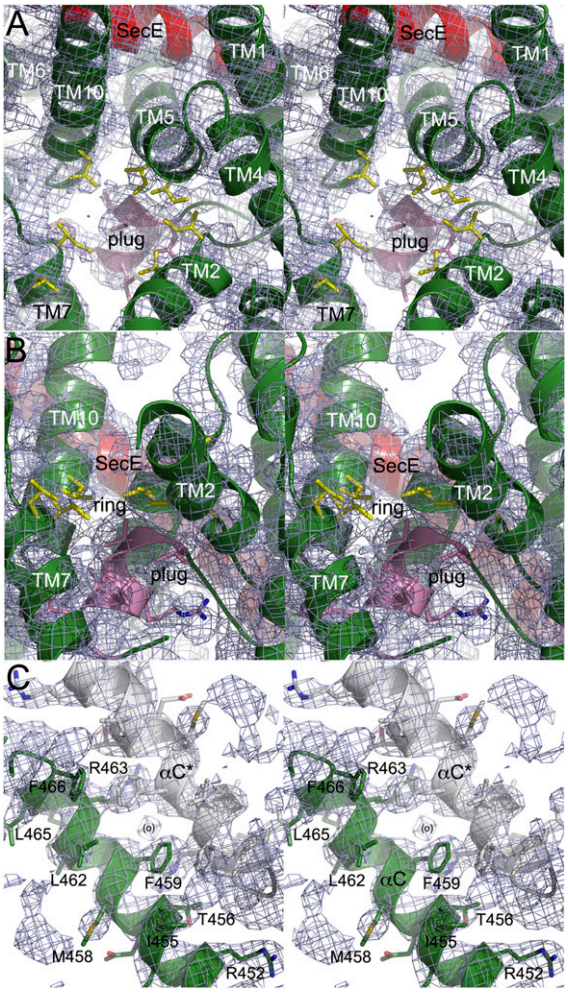

Fig. S3. Final electron density. Stereo views of the final likelihood-weighted 2mFo-DFc Fourier difference electron density map at 3.1-Å resolution contoured at 1.5σ. (*A* and *B*) The plug and ring regions are shown in two different orientations; a top cytoplasmic view in *A* and a lateral view facing the lateral gate in *B*. (*C*) The αC-terminal region of *Pfu*-SecY with the symmetry-related helix (labeled αC*) acting as a substrate mimic inserted in the channel vestibule. Helices are labeled using the same code as in Fig. S1. Side chains constituting the plug, ring, and αC-helix are displayed.

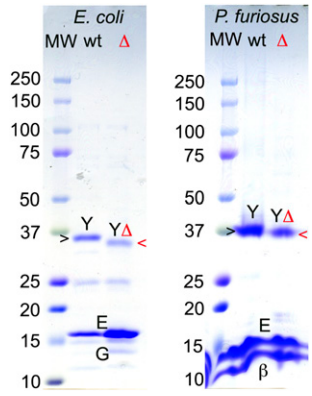

Fig. S4. Wild-type and C-terminal truncated forms of *P. furiosus* or *E. coli* translocons coexpress and associate into stable complexes in *E. coli* membranes. *E. coli*-SecYEG and *Pfu*-SecYEβ complexes coexpressed in *E. coli* were, respectively, purified in DDM and OG. SDS-stained PAGE gel showing the copurified complexes using histidine-tagged SecE subunits after a crude metal-chelating affinity chromatography step. The bands corresponding to the SecY subunits are identified with arrows. The wild-type (wt) and shorter C-terminally truncated (Δ) SecY subunits display notably different electrophoretic motilities. The E and β subunits from *Pfu*-SecY always migrate as broad bands at the front of the gel.

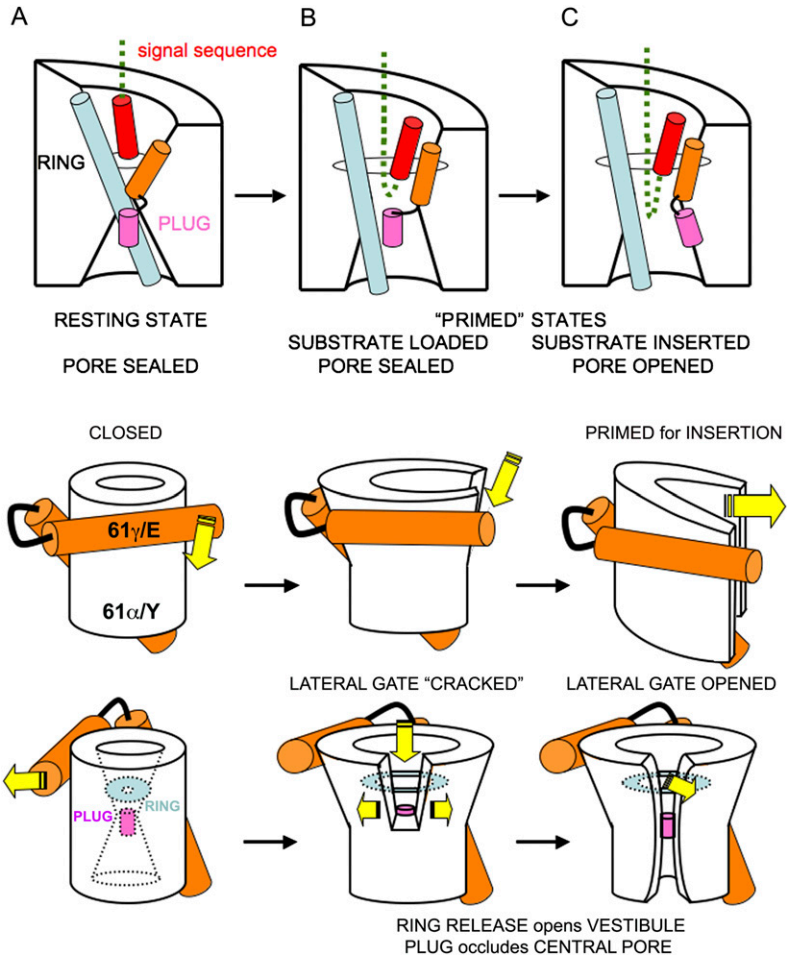

Fig. S5. Model for the path followed by a nascent chain during initial steps of translocation. The translocon undergoes a sequence of conformational changes. (*A*) In the resting state, the plug helix is in position and obstructs the pore, whereas the ring maintains a tight seal. (*B*) As a nascent chain enters the cytoplasmic vestibule, it docks against a surface constituted by helices α12 and α12 and sheets β1 and β2; we suggest that signal sequences interact with the C-terminal helix αC. However, in this primed state, the plug stays in place, despite the opening of the lateral gate. This might allow the nascent chain to adopt the correct orientation relative to its N and C termini and determine the final and correct topology of insertion into the membrane. (*C*) As the translocated substrate inserts farther into the pore, domain movements unlock the plug and widen the ring. The protein-conducting channel is open. Steps *A* and *C* were originally proposed by the group of Tom Rapoport (1). Step *B* is based on this work. A schematic of the three representative conformational states is shown, emphasizing (*i*) the progressive opening of the lateral gate, (*ii*) the release of the ring seal associated with the widening of the cytoplasmic vestibule, and (*iii*) the role of the plug as it still occludes the central pore.

1. Li W, et al. (2007) The plug domain of the SecY protein stabilizes the closed state of the translocation channel and maintains a membrane seal. *Mol Cell* 26:511–521.

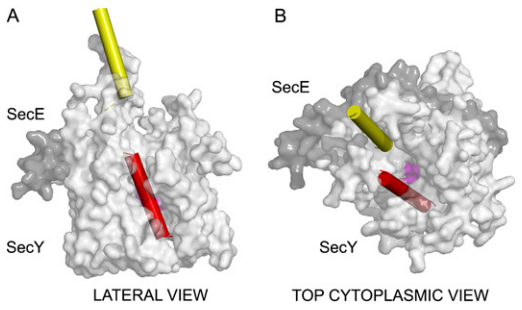

Fig. S6. Model of the translocation channel with a nascent chain docked in its vestibule and at the lateral gate. The N terminus of a nascent chain was modeled as a poly-leucine α-helical peptide that mimics a signal sequence (first TM in red) and another folded helix (at last partially) that represents a second TM (in yellow) about to be transferred to the channel. In our model, the first TM has already undergone the inversion that, in most cases, results in the N terminus of the substrate protein being exposed on the cytoplasmic side (thus, using the positive-inside rule). The *Pfu*-SecYE channel is rendered as a transparent envelope; our crystalline conformation can accommodate such a substrate. Two views are shown to emphasize (*A*) the accessibility of the lateral gate to a bona fide TM segment and (*B*) the size of the cytoplasmic vestibule, which is wide enough to accommodate partially folded intermediates. In the present model, the open space in the vestibule is large enough to accommodate another TM segment, suggesting that, in this conformation, the channel can support signal sequence inversion.

Table S1. X-ray data and structure refinement general statistics

Structure	*Pfu*-SecYE (ALS051007)			*Pfu*-SecYE (ALS071208)
Dataset data statistics				
Space group		$C222_1$		$C222_1$
Cell dimensions		*a* = 70.03 Å *b* = 136.71 Å *c* = 229.61 Å		*a* = 71.24 Å *b* = 141.68 Å *c* = 235.56 Å
ASU content		1 SecYE complex		1 SecYE complex
Solvent content		70%		72%
Phasing method		Se-MAD/MR		MR
	Inflection	Peak	Remote	
Wavelength	0.97966 Å	0.97958 Å	0.96863 Å	1.115872 Å
Resolution	50–3.5 Å	50–3.5 Å	50–3.5 Å	78.57–3.14 Å
Unique reflections (last shell)	13,149 (1,129)	13,058 (842)	13,209 (1,108)	20,830 (2,645)
Redundancy	3.8 (3.1)	3.7 (2.6)	3.7 (3.0)	3.9 (3.2)
Completeness	92% (81%)	86% (56%)	91% (79%)	98% (87%)
Mean $I/\sigma(I)$	13.6 (1.1)	11.2 (1.1)	14.2 (1.1)	9.8 (1.3)
R_{sym}	5.6% (63.7%)	5.6% (44.8%)	5.1% (61.2%)	6.5% (67.2%)
Refinement and validation				PDB ID: 3MP7
Resolution range		50–3.5 Å		50–2.9 Å overall
Reflections used work (test)		10,905 (538)		15,207 (1,375)
R_{free}/R_{cryst}		39.3%/37.5%(one cycle of building and refinement)		31.7%/27.7% (anisotropic correction); 38.0%/35.3% (no anisotropic correction)
Initial figure of merit (*solve*)		0.35		—
Initial figure of merit (*resolve*)		0.66		—
Final overall figure of merit		0.70(against experimental phases)		—
Estimated overall B_{wilson}		130 Å^2		90 Å^2 (anisotropic correction); 120 Å^2 (no anisotropic correction)
Protein atoms		—		3,371
Solvent atoms		—		None
R.m.s.d. bonds		—		0.010 Å
R.m.s.d. angles		—		1.27°
MolProbity analysis*		—		100th percentile—all atoms contact analysis 96th percentile—protein geometry
Ramachandran analysis		—		84% in preferred regions 12% in allowed regions 4% outliers

R.m.s.d, root mean square deviation from ideal geometry; MR, phasing using molecular replacement; Se-MAD, phasing performed using multiple wavelength anomalous dispersion of selenium; ASU, asymmetric unit. $R_{sym} = \Sigma_{hkl}\Sigma_i|I_{hkl,I} - \langle I_{hkl,i}\rangle|/\Sigma_{hkl}\Sigma_i|I_{hkl,i}|$ where $\langle I_{hkl,i}\rangle$ is the average intensity of the multiple hkl,i observations for symmetry-related reflections. $R_{cryst} = \Sigma||F_{obs}| - |F_{calc}||/\Sigma|F_{obs}|$. F_{obs} and F_{calc} are observed and calculated structure factors, R_{free} is calculated from a set of randomly chosen 5–8% reflections, and R_{cryst} is calculated over the remaining 92–95% of reflections. For the initial Se-MAD/MR dataset, the refinement statistics and the final overall figure of merit represent the overall quality of the model after a single cycle of manual building and refinement against experimental (nonmodified) phases.

*The 100th percentile is the best among structures of comparable resolution; the 0th percentile is the worst.

Table S2. Native X-ray data statistics: Statistics for reflections with *I/σ(I)> 0.0*

Resolution (Å)	Observed reflections	Unique reflections	Multiplicity [*I/σ(I) > 0.0*]	Completeness (%)	*Rsym* (%)	*I/σ(I)*	*Rmeas* (%)	*Rmerge-F* (%)
50.0–12.96	1,921	301	6.4	85.5	1.7	71.30	1.9	0.9
12.96–9.16	4,458	590	7.6	100	2.0	74.01	2.1	1.0
9.16–7.48	5,663	745	7.6	98.9	2.6	64.74	2.8	1.4
7.48–6.48	6,735	851	7.9	99.0	3.6	48.71	3.8	2.2
6.48–5.80	8,006	985	8.1	98.9	5.0	36.04	5.4	3.6
5.80–5.29	8,536	1,041	8.2	98.1	5.4	31.93	5.7	4.2
5.29–4.90	9,339	1,140	8.2	97.3	4.9	31.41	5.3	4.8
4.90–4.58	10,014	1,211	8.3	97.3	5.6	28.28	6.0	5.3
4.58–4.32	10,549	1,278	8.3	95.6	7.4	22.81	7.9	7.4
4.32–4.10	10,511	1,263	8.3	91.4	9.7	17.90	10.3	10.3
4.10–3.91	10,977	1,314	8.4	89.9	14.3	12.58	15.2	16.8
3.91–3.74	11,013	1,312	8.4	86.7	23.1	8.70	24.6	25.1
3.74–3.59	11,474	1,356	8.5	85.8	30.7	6.61	32.8	32.7
3.59–3.46	11,502	1,362	8.4	82.6	46.5	4.62	49.5	46.6
3.46–3.35	10,594	1,304	8.1	75.6	57.4	3.60	61.3	59.3
3.35–3.24	8,283	1,178	7.0	67.4	70.3	2.68	75.7	76.8
3.24–3.14	6,137	962	6.4	52.7	63.7	2.61	69.3	79.3
3.14–3.05	5,117	832	6.2	45.2	76.1	2.23	83.2	100.0
3.05–2.97	4,314	729	5.9	38.0	90.9	1.93	99.5	97.3
2.97–2.90	3,442	657	5.2	33.0	91.4	1.72	101.1	108.4
Overall	158,585	20,411	7.8	75.6	6.2	19.76	6.6	14.2

Rmeas is a redundancy-independent *Rsym. Rmerge-F* is an indicator of amplitude quality (1).

1. Diederichs K, Karplus PA (1997) Improved R-factors for diffraction data analysis in macromolecular crystallography. *Nature Struct Mol Biol* 4:269–275.

Table S3. Native X-ray data statistics: Statistics for reflections with *I/σ(I)> -3.0*

Resolution (Å)	Observed reflections	Unique reflections	Multiplicity [*I/σ(I) > −3.0*]	Completeness (%)	*Rsym* (%)	*I/σ(I)*	*Rmeas* (%)	*Rmerge-F* (%)
50.0–12.96	1,921	301	6.4	85.5	1.7	71.30	1.9	0.9
12.96–9.16	4,458	590	7.6	100.0	2.0	74.01	2.1	1.0
9.16–7.48	5,695	751	7.6	99.7	2.6	64.21	2.8	1.5
7.48–6.48	6,779	858	7.9	99.8	3.6	48.30	3.9	2.3
6.48–5.80	8,078	997	8.1	100.0	5.1	35.60	5.4	3.7
5.80–5.29	8,660	1,060	8.2	99.9	5.4	31.93	5.8	4.6
5.29–4.90	9,582	1,172	8.2	100.0	5.0	31.35	5.4	5.5
4.90–4.58	10,014	1,244	8.3	100.0	5.8	30.54	6.1	6.0
4.58–4.32	10,285	1,336	8.3	99.9	7.6	27.51	8.8	8.8
4.32–4.10	10,971	1,382	8.3	100.0	10.6	21.79	11.3	13.4
4.10–3.91	11,506	1,461	8.4	100.0	15.9	16.30	17.0	21.9
3.91–3.74	12,661	1,513	8.4	100.0	26.7	11.24	28.5	34.4
3.74–3.59	13,279	1,581	8.5	99.9	36.0	7.45	38.4	44.6
3.59–3.46	13,792	1,649	8.4	100.0	57.5	5.58	61.4	68.3
3.46–3.35	13,865	1,716	8.1	99.4	78.5	3.69	83.9	99.2
3.35–3.24	11,323	1,651	7.0	94.5	105.6	2.57	114.0	148.8
3.24–3.14	9,317	1,485	6.4	81.3	113.6	1.41	123.7	191.2
3.14–3.05	8,009	1,332	6.2	72.4	146.3	1.08	160.1	269.5
3.05–2.97	6,941	1,222	5.9	63.6	194.2	0.83	213.4	306.6
2.97–2.90	5,330	1,050	5.2	52.8	182.6	0.79	202.8	301.5
Overall	184,613	20,411	7.8	90.2	7.1	19.76	7.7	21.4

Rmeas is a redundancy-independent *Rsym. Rmerge-F* is an indicator of amplitude quality (1).

1. Diederichs K, Karplus PA (1997) Improved R-factors for diffraction data analysis in macromolecular crystallography. *Nature Struct Mol Biol* 4:269–275.

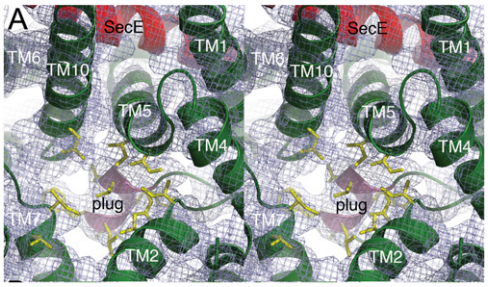

Movie S1. Experimental phasing and positioning of transmembrane helices of the *Pfu*-SecYE complex. The *Pfu*-SecYE structure is shown with the Y and E subunits colored using a progressive rainbow pattern as in Fig. 1. The likelihood-weighted *2mFo-DFc* Fourier difference initial electron density map at 3.5-Å resolution contoured at 1.1σ is displayed on the whole structure to emphasize correction positioning of all TM-spanning helices, particularly, TMs 2/3 and 7/8, that define the lateral gate and the C-terminal αC-helix. The selenium sites are shown as magenta spheres. The protein trace shown here is the result of a single round of model building against the experimental phases.

Movie S1

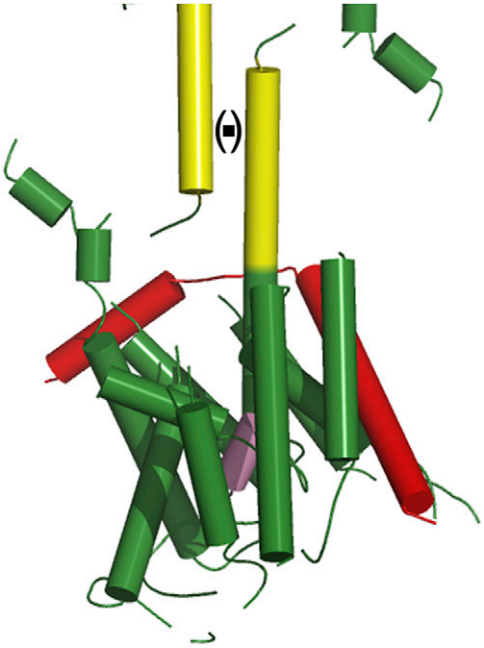

Movie S2. Overall arrangement of the *Pfu*-SecYE showing the opening of its lateral gate. Surface representation of the *Pfu*-SecYE structure with its Y and E subunits colored using a progressive rainbow pattern as in Fig. 1. The neighboring C-terminal αC-helix contributed by a symmetry-related SecYE complex (labeled αC*) is colored as a white surface to emphasize its insertion in the cytoplasmic vestibule of the channel. Because of the opening of the lateral gate in SecY along TMs 2/3 and 7/8, the plug helix can be seen. The surface representation also emphasizes the lateral opening of the channel and the three cytoplasmic insertions overlooking the cytoplasmic vestibule of the channel.

Movie S2

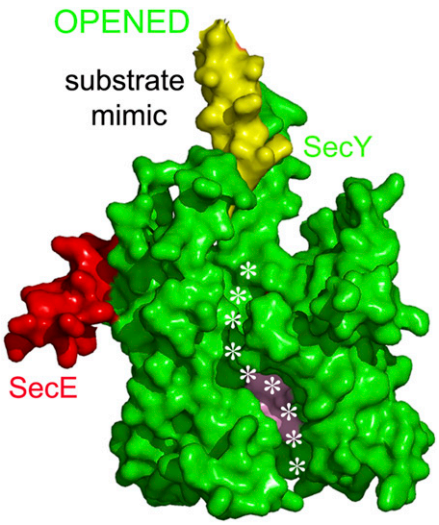

Movie S3. Superposition of the three known translocon structures emphasizing conformational changes. The structures of the *Mja*-SecYEβ, *Thermus thermophilus* (*Tth*)-SecYE, and *Pfu*-SecYE are sequentially displayed using ribbon or surface representations to emphasize the conformational rearrangements. The subunits SecY, SecE, or Sec61β are, respectively, colored in green, red, and white. The plugs are colored in pink.

Movie S3